



Cite this: *Phys. Chem. Chem. Phys.*,
2016, 18, 1507

Benzodi(pyridothiophene): a novel acceptor unit for application in A_1 – A – A_1 type photovoltaic small molecules†

Jianhua Chen,^a Manjun Xiao,^{ab} Linrui Duan,^a Qiong Wang,^a Hua Tan,^a Ning Su,^a Yu Liu,^a Renqiang Yang^{*b} and Weiguo Zhu^{*a}

A series of novel A_1 – A – A_1 type small molecules (SMs) of **BDPT-2BT**, **BDPT-2FBT** and **BDPT-2DPP** were designed and synthesized, in which benzodi(pyridothiophene) (**BDPT**) was used as a novel weak central acceptor (A) unit, and benzothiadiazole (BT), fluorinated benzothiadiazole (FBT) and diketopyrrolopyrrole (DPP) were used as terminal acceptor (A_1) units, respectively. The pentacyclic **BDPT** aromatic unit can form big conjugated and planar SMs with the A_1 unit, resulting in enhanced π – π stacking and crystallinity. The effect of the A_1 unit on the optical, electrochemical and photovoltaic properties of three SMs was observed. The broader absorption spectrum, lower HOMO energy level, higher photo-response efficiency and better photovoltaic properties were exhibited for **BDPT-2DPP**. A maximum PCE of 3.97% with a V_{oc} of 0.84 V, a J_{sc} of 9.0 mA cm^{–2} and a FF of 52.37% was obtained in the **BDPT-2DPP**/PC₇₁BM-based solar cells, which is 1.8 and 1.5 times the values of the **BDPT-2BT** and **BDPT-2FBT**-based cells, respectively.

Received 13th September 2015,
Accepted 20th November 2015

DOI: 10.1039/c5cp05474e

www.rsc.org/pccp

1. Introduction

For developing high-efficiency organic photovoltaics (OPVs), in the past few years, many building blocks of benzodithiophene, fluorene, carbazole, thienopyrrolodione, quinoxaline, diketopyrrolopyrrole, benzothiadiazole and isoindigo have been widely used to construct photovoltaic donor materials.^{1–10} The modification and improvement of these building blocks, such as fluorination, atom substitution, fused ring-expanding, side chain engineering and so on, have been found to promote the photovoltaic performance for their polymers and small molecules.^{11–18} Consequently, the power conversion efficiency (PCE) of 10.7%¹⁹ and 10.1%²⁰ for OPVs based on polymers (P-OPVs) and small molecules (SM-OPVs) have been achieved, respectively.

Among these building blocks, the lactam derivatives were mostly reported as acceptor units in photovoltaic materials owing to their strong electron-withdrawing ability for forming the intramolecular donor–acceptor electron transfer and the relatively strong interaction between amide groups and fullerenes for

efficient charge carrier separation.^{21–23} As a result, polymers bearing lactam units have shown excellent photovoltaic performance in P-OPVs. For instance, Marks *et al.* reported a series of bithiopheneimide (BTI)-based polymers and presented a maximum PCE of 6.41% for their OPVs.²¹ The Ding group designed a new pentacyclic aromatic lactam (TPTI) as the acceptor unit and exhibited a PCE of 7.80% for the TPTI-based polymer in OPVs.²³

As lactam with ambident reactivity is easily functionalized by *N*- or *O*-alkylation, Kroon *et al.* recently presented an isomer of the tetracyclic lactam (NT) building block by *O*-alkylation, which is also regarded as a pyridine derivative, and its copolymer showed a PCE of 5% in OPVs.²⁴ Liu *et al.* developed a thiophene-fused aza-coronene (TAC) unit with a bigger conjugate and planar system and its copolymer with a mobility up to 0.028 cm² V^{–1} s^{–1} and a PCE of 4.8% in the inverted device.²⁵ Both fused heterocyclic building blocks of NT and TAC have low electron-withdrawing ability because of the effect of the nitrogen atom with sp² hybridization in the fused-pyridine rings, which help its copolymers achieve deep highest occupied molecular orbital (HOMO) and its OPV devices to obtain high open circuit voltage (V_{oc}). Furthermore, these copolymers containing NT and TAC units have remarkable self-organization behavior, which promotes their OPV devices to exhibit a high fill factor (FF). However, these OPV devices have not exhibited satisfactory short circuit density (J_{sc}) and PCE values. This is considered to be related to the relatively narrow absorption spectra of these copolymers. Thus, the broader UV-vis absorption spectra with low band-gap and suitable energy levels are needed for the copolymers.

^a College of Chemistry, Xiangtan University, Key Lab of Environment-Friendly Chemistry and Application in Ministry of Education, Xiangtan 411105, China. E-mail: zhuwg18@126.com

^b Qingdao Institute of Bioenergy and Bioprocess Technology, Chinese Academy of Sciences, Qingdao 266101, China. E-mail: yangrq@qibebt.ac.cn

† Electronic supplementary information (ESI) available: The detailed data of the optimal BHJ solar cells and their corresponding *J*–*V* curves, the NMR spectra, MALDI-MS data and crystal data. CCDC 1412263. For ESI and crystallographic data in CIF or other electronic format see DOI: 10.1039/c5cp05474e

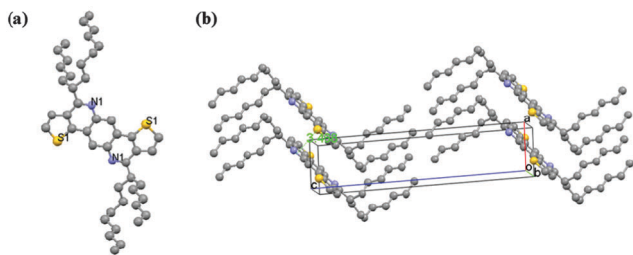


Fig. 1 Crystal structure of **BDPT** (a) and the intermolecular arrangements in the crystal (b). H-atoms are omitted for clarity.

SM-OPVs have many advantages, such as well-defined structures, easier purification, and less batch to batch variation, as compared to P-OPVs. In this work, we focused on a multi-heterocyclic building block to construct novel photovoltaic small molecules with broad UV-vis absorption spectra and suitable energy levels. Herein, a novel penta-heterocyclic building block of benzodi(pyridothiophene) (**BDPT**), *i.e.* thieno[2',3':4,5]pyrido[2,3-*g*]thieno[3,2-*c*]quinoline (Fig. 1) was designed and synthesized *via* Bischler–Napieralski cyclization. In consideration of the intrinsic relatively low HOMO energy level of the pyridine derivative and the requirement of broad absorption spectra for photovoltaic SMs, a series of A_1 – A_1 type SMs of **BDPT-2BT**, **BDPT-2FBT** and **BDPT-2DPP** were designed and synthesized, in which **BDPT** was used as a weak central acceptor (A) unit and benzothiadiazole (BT), fluorinated benzothiadiazole (FBT), and diketopyrrolopyrrole (DPP) were used as the second strong acceptor (A_1) unit, respectively. In this case, the optical, electrochemical and photovoltaic properties of these SMs can be tuned with the second acceptor unit. As expected, these three SMs showed enhanced π – π stacking and crystallinity, as well as relatively low HOMO energy levels. **BDPT-2DPP** exhibited a broader absorption spectrum, lower HOMO energy level, higher photo-response efficiency and better photovoltaic property in contrast to **BDPT-2BT** and **BDPT-2FBT**. A maximum PCE of 3.97% with a V_{oc} of 0.84 V, a J_{sc} of 9.0 mA cm $^{-2}$ and a FF of 52.37% was obtained in the **BDPT-2DPP**/PC $_{71}$ BM-based solar cells. Our results demonstrated that benzodi(pyridothiophene) is a promising building block to construct photovoltaic SMs for potential application in solution-processed SM-OPVs.

2. Experimental section

2.1. Materials

All reactions were carried out under a nitrogen atmosphere. All reagents and solvents were purchased from Adamas, and Sigma and Aldrich corporations. These chemicals were used without further purification unless stated otherwise. Compounds 2–7 and 9–11 were prepared according to the reported procedures.^{26–29}

2.2. Measurement and characterization

^1H NMR and ^{13}C NMR spectra were recorded on a Bruker Avance-400 spectrometer at 400 MHz and 100 MHz using CDCl_3 as the solvent and tetramethylsilane (TMS) as the internal standard unless specified otherwise, respectively. Mass spectra were measured on a Bruker Daltonics BIFLEX III MALDI-TOF analyzer using

the MALDI-TOF mode. Crystal-structures were determined on a Nonius KCCD diffractometer with graphite monochromated Mo K radiation. The structures were analyzed by direct methods (SHELXS-97). UV-vis absorption spectra were recorded on a Shimadzu UV-1800 spectrophotometer. Thermogravimetric analysis (TGA) was measured on a Perkin-Elmer Diamond TG/DTA thermal analyzer at a scan rate of 10 $^\circ\text{C min}^{-1}$ under a nitrogen atmosphere. The differential scanning calorimetry (DSC) was measured on a TA DSCQ-10 instrument at a heating rate of 10 $^\circ\text{C min}^{-1}$ under a nitrogen atmosphere. The cyclic voltammetry (CV) measurement was conducted on a CHI620 voltammetric analyzer under an argon atmosphere in an anhydrous acetonitrile solution of tetra(*n*-butyl) ammonium hexafluorophosphate (0.1 M) at a scan rate of 20 mV s $^{-1}$. A platinum plate, a platinum wire and an Ag/AgCl electrode were used as the working electrode, counter electrode, and reference electrode, respectively. SMs were coated on the surface of the platinum plate and all potentials were corrected against Fc/Fc^+ .

2.3. Device fabrication and characterization

All devices were fabricated on indium tin oxide (ITO)-coated glass substrates, which were cleaned by ultrasonic wave with detergent, deionized water, acetone, and isopropyl alcohol, for 20 min. Poly(3,4-ethylenedioxythiophene)/poly(styrenesulfonate) (PEDOT:PSS, CleviosTM P Al 4083) was spin-coated onto ITO glass at 4000 rpm for 30 s and baked at 150 $^\circ\text{C}$ for 10 min in air. The solution of SM and PC $_{71}$ BM in chloroform (12 mg mL $^{-1}$) was spin-coated onto the PEDOT:PSS layer to form the active layer. The thickness of the active layer was approximately 90 nm, measured by a KLA Tencor D-120 profilometer. Ca (10 nm) and Al (100 nm) were deposited successively on the active layer by thermal evaporation under a vacuum less than 2×10^{-6} mbar. The active area was 4 mm 2 for each cell. Current density (J)–voltage (V) curves were performed on a Newport 150 W solar simulator under AM1.5G illumination with irradiation intensity of 100 mW cm $^{-2}$. The external quantum efficiency (EQE) of the devices was measured on a QE-R3011 solar spectral response measurement system (Enli Technology).

2.4. Synthesis

2.4.1 Synthesis of 2,5-di(thiophen-2-yl)-1,4-bis(2-hexyldecan-amido)phenylene (8). To a solution of 2,5-di(thiophen-2-yl)-benzene-1,4-diamine (1.2 g, 44.1 mmol) in THF/Et $_3\text{N}$ (v/v, 1:1), 2-hexyldecanoyl chloride (4.8 g, 175.2 mmol) was added slowly at 0 $^\circ\text{C}$ under stirring. The mixture was then stirred at room temperature for 2 h and poured into water (80 mL). The organic phase was separated and the aqueous solution was extracted with dichloromethane (2×50 mL). The resulting organic layers were combined and dried over anhydrous MgSO_4 . The organic solvent was distilled off and the residue was purified by chromatography on a silica gel column using a mixture of dichloromethane (CH_2Cl_2) and petroleum ether (PE) (v/v, 1:1) as eluent to afford compound **8** as a white solid (2.1 g, 63.6%). ^1H NMR (400 MHz, CDCl_3) δ (ppm): 8.45 (s, 2H), 7.48 (s, 2H), 7.45 (d, J = 3.8 Hz, 4H), 7.19 (s, 2H), 7.15 (d, J = 3.7 Hz, 2H), 2.05 (s, 2H), 1.42 (s, 8H), 1.24 (s, 40H), 0.86 (s, 12H). ^{13}C NMR (100 MHz, CDCl_3) δ (ppm): 174.38,

138.44, 131.28, 127.75, 127.50, 127.00, 125.00, 123.62, 49.30, 33.18, 31.85, 31.70, 29.70, 29.46, 29.36, 29.28, 27.66, 27.62, 22.66, 22.62, 14.10, 14.06. Elemental analysis for $C_{46}H_{72}N_2O_2S_2$: calcd C, 73.74; H, 9.69; N, 3.74; found C, 73.53; H, 9.38; N, 3.94.

2.4.2 Synthesis of 4,10-di(pentadecan-7-yl)thieno[2',3':4,5]-pyrido[2,3-g]thieno[3,2-c]quinoline (BDPT). Compound **8** (1.5 g, 2.0 mmol) and P_2O_5 (1 g, 8.9 mmol) in freshly distilled $POCl_3$ (40 mL) was stirred at reflux for 6 h under N_2 . The solvent was distilled under a high vacuum, the residue was cooled to room temperature and transferred slowly to ice water (100 mL). The mixture was adjusted to pH = 10 with NaOH solution (2 M) and then extracted with $CHCl_3$ (3×30 mL). The combined organic layers were dried over anhydrous $MgSO_4$ and distilled to remove the solvent. The residue was purified by chromatography on a silica gel column using CH_2Cl_2 -PE (v/v, 1:5) as eluent and recrystallized from ethanol to afford **BDPT** as a light yellow solid (1.1 g, 77.0%). 1H NMR (400 MHz, $CDCl_3$) δ (ppm): 8.92 (s, 2H), 7.72 (d, J = 5.2 Hz, 2H), 7.60 (d, J = 5.2 Hz, 2H), 3.42 (dd, J = 12.0, 6.7 Hz, 2H), 2.18–2.05 (m, 6H), 1.92–1.70 (m, 10H), 1.23 (d, J = 32.3 Hz, 22 H), 0.82 (t, J = 6.3 Hz, 12H). ^{13}C NMR (100 MHz, $CDCl_3$) δ (ppm): 163.28, 144.96, 141.64, 133.30, 125.74, 124.02, 123.98, 122.90, 46.32, 35.14, 35.12, 31.82, 31.70, 29.84, 29.52, 29.42, 29.20, 27.96, 27.94, 22.58, 22.56, 13.98, 13.96. MS (MALDI-TOF) for $C_{46}H_{68}N_2S_2$: 714.525 $[M + H]^+$. Elemental analysis for $C_{46}H_{68}N_2S_2$: calcd C, 77.47; H, 9.61; N, 3.93; found C, 74.08; H, 9.97; N, 3.77.

2.4.3 Synthesis of 4,10-di(pentadecan-7-yl)-2,8-bis(trimethylstannyl)thieno[2',3':4,5]pyrido[2,3-g]thieno[3,2-c]quinoline (M1). To a solution of compound **BDPT** (1.4 g, 2.0 mmol) in THF (100 mL) at $-78^\circ C$, 2 mL of *n*-butyllithium (4.4 mmol, 2.5 M in *n*-hexane) was added dropwise under stirring and a nitrogen atmosphere. After being stirred at $-78^\circ C$ for 1 h, a great deal of yellow solid precipitate appeared. Then, 4.4 mL of trimethyltin chloride (4.4 mmol, 1 M in *n*-hexane) was added in one portion, and the mixture rapidly turned clear. After allowing it to warm to ambient temperature, the reactant was stirred for 2 h. It was poured into 200 mL of cool water and the mixture was extracted by ether (3×50 mL). The organic layer was washed with water two times and then dried over anhydrous $MgSO_4$. After removal of the solvent under vacuum, the residue was recrystallized using ethanol and compound **M1** was obtained as a pale yellow crystal (1.5 g, yield 72.5%). 1H NMR (400 MHz, $CDCl_3$) δ (ppm): 8.93 (s, 2H), 7.80–7.70 (m, 2H), 3.48 (s, 2H), 2.09 (t, J = 21.8 Hz, 6H), 1.86 (s, 6H), 1.60–1.16 (m, 36H), 0.89–0.73 (m, 12H), 0.48 (d, J = 28.2 Hz, 18H). ^{13}C NMR (100 MHz, $CDCl_3$) δ (ppm): 163.92, 149.86, 141.26, 139.88, 134.66, 131.64, 123.78, 123.06, 46.08, 35.08, 35.04, 31.88, 31.76, 29.92, 29.58, 29.48, 29.28, 27.94, 27.92, 22.64, 22.62, 14.08, 14.06, -8.04 . MS (MALDI-TOF) for $C_{52}H_{84}N_2S_2Sn_2$: 1039.465 $[M + H]^+$. Elemental analysis for $C_{52}H_{84}N_2S_2Sn_2$: calcd C, 60.12; H, 8.15; N, 2.70; found C, 60.12; H, 7.94; N, 2.82.

2.4.4 Synthesis of BDPT-2BT. To a solution of compound **9** (164.4 mg, 0.3 mmol) and **M1** (155.7 mg, 0.15 mmol) in toluene (10 mL) were added tris(dibenzylideneacetone)dipalladium ($Pd_2(dba)_3$, 6 mg) and tri-*o*-tolylphosphine (12 mg) under a nitrogen atmosphere. The mixture was stirred at $110^\circ C$ for 6 h. After allowing

the reaction solution to cool to ambient temperature, the mixture was poured into 100 mL water and extracted with CH_2Cl_2 (100 mL). The resulting organic phase was collected and dried over anhydrous $MgSO_4$. After the solvent was distilled by rotary evaporation, the residue was purified by chromatography on a silica gel column using CH_2Cl_2 -PE (v/v, 3:1) as eluent to give a red solid (202.2 mg, yield 82.1%). 1H NMR (400 MHz, $CDCl_3$) δ (ppm): 8.85 (s, 2H), 8.04 (d, J = 12.0 Hz, 4H), 7.88 (s, 4H), 7.74 (s, 2H), 7.08 (s, 2H), 3.52 (s, 2H), 3.03 (s, 4H), 2.72 (s, 4H), 2.22 (s, 4H), 2.04–0.99 (m, 76H), 0.99–0.86 (m, 24H). MS (MALDI-TOF) for $C_{98}H_{128}N_6S_8$: 1647.125 $[M + H]^+$. Elemental analysis for $C_{98}H_{128}N_6S_8$: calcd C, 71.48; H, 7.84; N, 5.10; found C, 71.72; H, 7.71; N, 5.12.

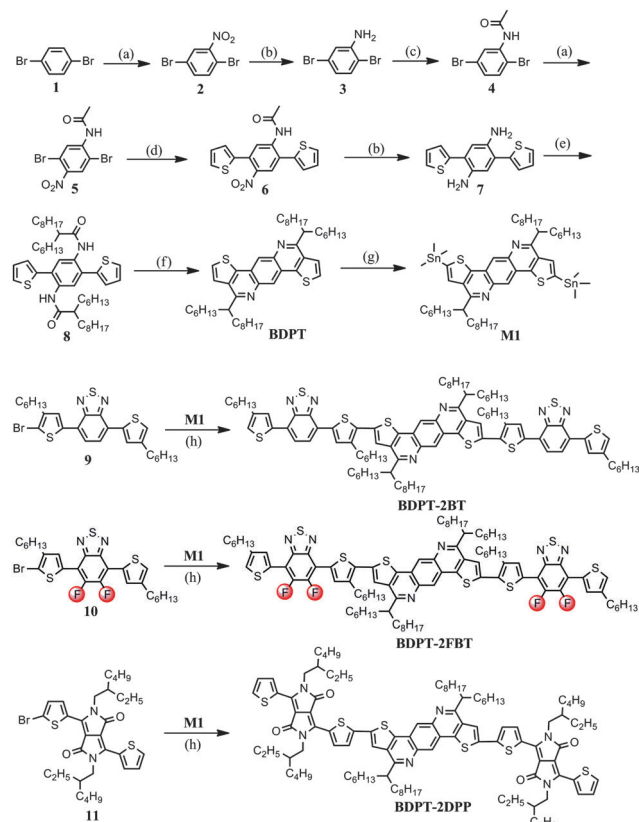
2.4.5 Synthesis of BDPT-2FBT. To a solution of compound **10** (175.2 mg, 0.3 mmol) and **M1** (155.7 mg, 0.15 mmol) in toluene (10 mL) were added $Pd_2(dba)_3$ (6 mg) and tri-*o*-tolylphosphine (12 mg) under a nitrogen atmosphere. The synthetic procedures were the same as for the synthesis of **BDPT-2BT**. The product was purified by chromatography on a silica gel column using CH_2Cl_2 -PE (v/v, 2.5:1) as eluent to give a red solid (201.5 mg, yield 78.2%). 1H NMR (400 MHz, $CDCl_3$) δ (ppm): 8.52 (s, 2H), 8.08 (s, 2H), 8.01 (s, 2H), 7.43 (s, 2H), 7.05 (s, 2H), 3.48–3.41 (m, 2H), 2.96 (t, J = 7.2 Hz, 4H), 2.60 (t, J = 6.8 Hz, 4H), 2.24 (d, J = 6.0 Hz, 4H), 1.98 (s, 4H), 1.86 (dd, J = 14.5, 7.4 Hz, 4H), 1.62 (s, 10H), 1.54–1.20 (m, 54H), 1.00 (t, J = 6.5 Hz, 6H), 0.92–0.83 (m, 18H). MS (MALDI-TOF) for $C_{98}H_{128}F_4N_6S_8$: 1719.297 $[M + H]^+$. Elemental analysis for $C_{98}H_{128}F_4N_6S_8$: calcd C, 68.49; H, 7.27; N, 4.89; found C, 68.60; H, 7.31; N, 4.82.

2.4.6 Synthesis of BDPT-2DPP. To a solution of compound **11** (127.2 mg, 0.2 mmol) and **M1** (103.8 mg, 0.1 mmol) in toluene (10 mL) were added $Pd_2(dba)_3$ (5 mg) and tri-*o*-tolylphosphine (10 mg) under a nitrogen atmosphere. The synthetic procedures were the same as for the synthesis of **BDPT-2BT**. The product of **BDPT-2DPP** was purified by chromatography on a silica gel column using CH_2Cl_2 -PE (v/v, 2:1) as eluent to give a blue solid (126.1 mg, yield 72.2%). 1H NMR (400 MHz, $CDCl_3$) δ (ppm): 8.99 (d, J = 3.9 Hz, 2H), 8.92 (d, J = 3.2 Hz, 2H), 8.59 (s, 2H), 7.72 (s, 2H), 7.58 (d, J = 4.1 Hz, 2H), 7.41 (s, 2H), 7.24 (d, J = 4.1 Hz, 2H), 4.06 (d, J = 5.6 Hz, 8H), 3.43 (d, J = 5.5 Hz, 2H), 2.17 (d, J = 7.7 Hz, 4H), 1.93 (s, 10H), 1.50–1.10 (m, 70H), 0.99–0.68 (m, 36H). MS (MALDI-TOF) for $C_{106}H_{144}N_6O_4S_6$: 1758.075 $[M + H]^+$. Elemental analysis for $C_{106}H_{144}N_6O_4S_6$: calcd C, 72.93; H, 8.25; N, 4.78; found C, 72.53; H, 7.86; N, 4.49.

3. Results and discussion

3.1. Synthesis

The synthetic route of three SMs is shown in Scheme 1. Compound **7** was reacted with 2-hexyldecanoyl chloride in a mixing solvent of THF and Et_3N at $0^\circ C$ to give compound **8** with a moderate yield of 63%. The key intermediate of **BDPT** was obtained by a reaction between compound **8** and condensation reagents P_2O_5 and $POCl_3$ with a yield of 77%, which is called a Bischler-Napieralski cyclization. The structure of **BDPT** was characterized by single crystal X-ray diffraction. **M1** was synthesized



Scheme 1 Synthetic route of the **BDPT**-based SMs. (a) Con. H_2SO_4 , con. HNO_3 , 0°C ; (b) SnCl_2/HCl , CH_3OH , reflux; (c) $\text{CH}_3\text{OH}/\text{H}_2\text{O}$, $\text{CH}_3\text{COOCH}_3$, reflux; (d) 2-(tributylstannyl)thiophene, $\text{Pd}(\text{PPh}_3)_4$, toluene, 110°C ; (e) 2-hexyldecanoyl chloride, THF, Et_3N , 0°C ; (f) POCl_3 , P_2O_5 , 100°C ; (g) THF, -78°C , $n\text{-BuLi}$, Me_3SnCl ; (h) $\text{Pd}(\text{PPh}_3)_4$, toluene, 110°C .

from **BDPT** in the presence of $n\text{-BuLi}$ and Me_3SnCl at -78°C . The target SMs **BDPT-2BT**, **BDPT-2FBT** and **BDPT-2DPP** were synthesized *via* a Still coupling reaction of **M1** and compounds **9**, **10**, and **11** with yields over 70%. The structures of these target SMs were characterized by ^1H NMR, MS, and elemental analysis.

3.2. Crystal structure of BDPT

A single crystal of **BDPT** was grown by slow diffusion of MeOH into the concentrated **BDPT** solution in CHCl_3 . The crystal structure of **BDPT** was determined and the crystallographic data are provided in the ESI.† CCDC 1412263. As observed, **BDPT** belongs to the $P\bar{1}$ space group of the triclinic system with $\alpha = 84.894^\circ$, $\beta = 88.701^\circ$, and $\gamma = 72.509^\circ$. As shown in Fig. 1, **BDPT** exhibits good planarity and $\pi\text{-}\pi$ stacking with a distance of 3.468 \AA , which will promote charge transfer when used as a building block in photovoltaic materials.

3.3. Thermal properties

The thermal behavior of three **BDPT**-based SMs was evaluated by thermogravimetric analysis (TGA) and differential scanning calorimetry (DSC) measurement. Fig. 2a and b show the recorded TGA and DSC curves, respectively. The detailed data are outlined in Table S1 (ESI†). As depicted in Fig. 2a, the

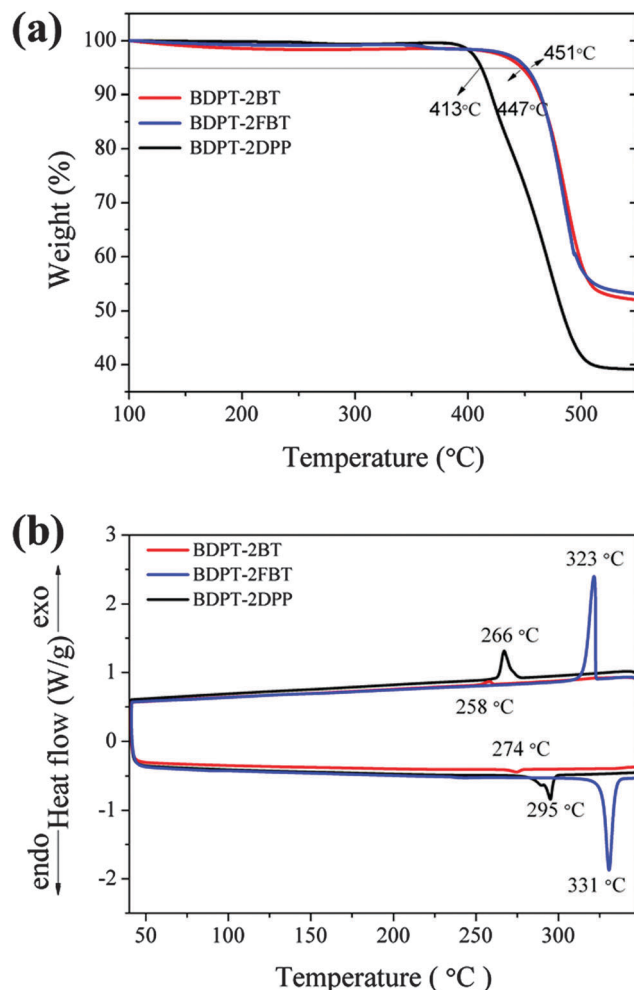


Fig. 2 TGA (a) and DSC (b) curves of the **BDPT**-based SMs.

decomposition temperature (T_d) at 447°C , 451°C and 423°C are observed for **BDPT-2BT**, **BDPT-2FBT** and **BDPT-2DPP** at 5% weight loss, respectively. These high T_d values may originate from the relatively high crystallinity and intermolecular interaction. On the other hand, an endothermic peak under the heating process and an exothermic peak under the cooling process are observed for the three **BDPT**-based SMs in Fig. 2b, which correspond to the melting temperature (T_m) and crystallization temperature (T_c), respectively. By comparison, it is found that both **BDPT-2FBT** and **BDPT-2DPP** exhibited significantly increased T_m and T_c than **BDPT-2BT**. Therefore, introducing an F atom and changing the second acceptor from a BT to a DPP unit have a significantly positive influence on thermal stability and crystallinity.

3.4. Optical properties

The UV-vis absorption spectra of **BDPT**-based SMs in chloroform solution (10^{-5} M) and in their thin films are shown in Fig. 3. The detailed data are outlined in Table 1. Two distinct absorption bands at a high-lying region from 300–400 nm and a low-lying region from 400–700 nm are observed for these **BDPT**-based SMs in solution and solid state. An absorption maximum

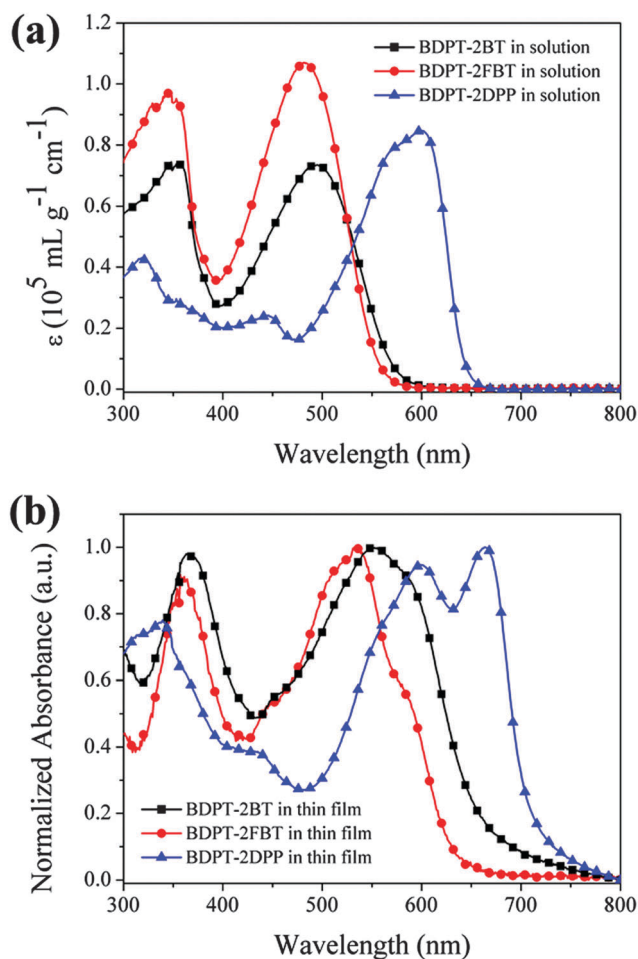


Fig. 3 UV-vis absorption spectra of the **BDPT**-based SMs in chloroform solution (a) and in thin films (b).

is displayed at 492 nm with a molar extinction coefficient (ϵ) of $7.2 \times 10^4 \text{ M}^{-1} \text{ cm}^{-1}$ for the **BDPT-2BT** solution and at 482 nm with a ϵ value of $1.02 \times 10^5 \text{ M}^{-1} \text{ cm}^{-1}$ for the **BDPT-2FBT** solution. Compared to **BDPT-2BT**, **BDPT-2FBT** shows a clear blue-shifted absorption profile in solution and solid state due to the electron-withdrawing effect of the fluorine atom.³⁰ When the BT unit is replaced by the DPP unit in the **BDPT**-based SMs, **BDPT-2DPP** shows a broader absorption profile than **BDPT-2BT** and **BDPT-2FBT**, due to the stronger electron-deficient ability of DPP than BT and FBT, which results in the stronger intramolecular charge transfer (ICT) effect. The absorption maximum appears at

600 nm, with an increasing ϵ value of $8.4 \times 10^5 \text{ M}^{-1} \text{ cm}^{-1}$ for **BDPT-2DPP** in solution. In contrast to the absorption profiles in solution, those in the neat films for these three **BDPT**-based SMs are remarkably red-shifted by about 60 nm due to the strong inter-molecular interactions. Furthermore, a new shoulder peak occurs in the long-wavelength for the three **BDPT**-based SMs, which results from vibronic coupling due to the rigid planar conjugated structure enforced by the molecular packing. The optical band gaps (E_g^{opt}) estimated from the absorption edges (652 nm, 630 nm, and 710 nm) of the thin films are 1.90, 1.97 and 1.75 eV for **BDPT-2BT**, **BDPT-2FBT** and **BDPT-2DPP**, respectively. As observed, the E_g^{opt} values of this kind of SMs were governed by the electron-deficient ability of the second acceptor units.

3.5. Electrochemical properties

The electrochemical properties of the **BDPT**-based SMs were evaluated by cyclic voltammetry (CV) method. The resulting CV curves are shown in Fig. 4 and their detailed data are summarized in Table 1. The reversible oxidation waves are observed with the onset oxidation potentials (E_{ox}) of 1.01 V, 1.18 V and 1.07 V vs. Ag/AgCl electrode for **BDPT-2BT**, **BDPT-2FBT** and **BDPT-2DPP**, respectively. However, the reductive waves did not appear. As the potential of the Fc/Fc^+ vs. Ag/AgCl electrode was measured to be 0.43 V in this work, the HOMO energy levels (E_{HOMO}) of the **BDPT**-based SMs can be calculated by the following equation: $E_{\text{HOMO}} = -(E_{\text{ox}} + 4.37) \text{ eV}$.³¹ As a result, the E_{HOMO} values of **BDPT-2BT**, **BDPT-2FBT** and **BDPT-2DPP** are -5.38 eV , -5.55 eV and -5.44 eV , respectively. Therefore, turning the second acceptor unit from BT to FBT and DPP can make their SMs exhibit lower HOMO energy levels.

3.6. Theoretical calculation

Optimal conformations of the three **BDPT**-based SMs were obtained by molecular modelling on Gaussian 09 at the B3LYP/6-31G* level of theory in the gas phase. To minimize the calculation process, the long alkyl chains were substituted with methyl groups during the calculation. The optimized molecular geometries are depicted in Fig. 5. The backbone of three SMs displays good planarity with a small torsion angle of 2.01° , 2.65° and 0.91° between the strong acceptor unit (BT, FBT and DPP) and the center **BDPT** unit for **BDPT-2BT**, **BDPT-2FBT** and **BDPT-2DPP**, respectively. The resulting planar structure can facilitate π - π stacking and charge transfer. The calculated frontier orbital distribution of the HOMO and the LUMO for SMs are presented in Fig. S1 (ESI[†]). For **BDPT-2BT** and **BDPT-2FBT**, the

Table 1 Optical and electro-chemical properties of the **BDPT**-based SMs

SM	λ_{max} (nm)		λ_{onset} (nm)	$E_g^{\text{opt } a}$ (eV)	E_{HOMO}^b (eV)	E_{LUMO}^c (eV)
	Solution ($\epsilon \times 10^4$)	Film				
BDPT-2BT	350 (9.5), 492 (10.2)	363, 556, 587	652	1.90	-5.38	-3.48
BDPT-2FBT	345 (7.4), 482 (7.2)	360, 537, 580	630	1.97	-5.55	-3.58
BDPT-2DPP	332 (4.3), 600 (8.4)	337, 600, 663	710	1.75	-5.44	-3.69

^a Calculated from the absorption band edge of the films, $E_g = 1240/\lambda_{\text{onset}}$. ^b Calculated from empirical equation: $E_{\text{HOMO}} = -(E_{\text{ox}} + 4.37) \text{ eV}$.

^c Calculated from $E_{\text{LUMO}} = E_{\text{HOMO}} + E_g^{\text{opt}}$.

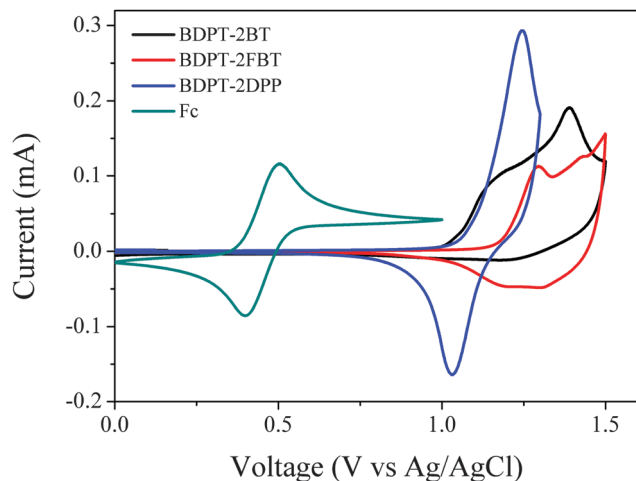


Fig. 4 CV curves of the **BDPT**-based SMs.

HOMOs are well delocalized along the backbones of SMs, while the LUMOs are localized on the second acceptors of the BT and FBT units. However, both HOMO and LUMO are delocalized along the backbones for **BDPT-2DPP**. As the localization can hinder interchain electron transport, since hopping requires good alignment of the localized LUMO levels,^{32–35} the stronger delocalization of both the HOMO and LUMO for **BDPT-2DPP** is expected to enhance intermolecular interactions and improve charge transportation than those for **BDPT-2BT** and **BDPT-2FBT**.

3.7. Photovoltaic properties

Bulk heterojunction (BHJ) solar cells based on SMs and PC₇₁BM were fabricated. The SM/PC₇₁BM ratios from 1 : 2, 1 : 1 to 2 : 1 and the solvent additive of 1,8-diiodooctane (DIO) from 0% to 1% were selected to optimize device performance in the active layer. Table S2 (ESI[†]) summarized the corresponding photovoltaic parameters of the SM/PC₇₁BM-based devices under illumination of AM1.5, 100 mW cm^{−2}. The corresponding *J*–*V* curves and the dark currents in the *J*–*V* curves for **BDPT**-based solar cells were displayed in Fig. S2–S4 (ESI[†]). It is found that the optimized SM/PC₇₁BM ratio is 1 : 1. The introduction of the 1% DIO additive improves the photovoltaic properties of the **BDPT-2DPP**-based devices, but decreases the photovoltaic properties of the **BDPT-2BT** and **BDPT-2FBT**-based devices. Fig. 6 shows the typical *J*–*V* curves of the SM:PC₇₁BM-based devices in this optimized SM/PC₇₁BM ratio and solvent additive conditions. We find that the **BDPT-2DPP**-based devices exhibited better photovoltaic properties than the **BDPT-2BT** and **BDPT-2FBT**-based devices. The maximum PCE of 3.09% with a *V*_{oc} of 0.84 V, a *J*_{sc} of 8.0 mA cm^{−2} and a FF of 52.37% was obtained in the **BDPT-2DPP**-based devices at the SM/PC₇₁BM ratio of 1 : 1. It indicates that turning the second acceptor unit from BT to FBT and DPP can improve the photo-voltaic property for these A₁–A–A₁ type SMs.

For further tuning photovoltaic properties of this type of SMs with an A₁–A–A₁ framework, the **BDPT-2DPP**-based device with the **BDPT-2DPP**/PC₇₁BM ratio of 1.5 : 1 and 1% DIO additive was specially made. The increasing PCE of 3.97% with a *V*_{oc} of 0.84 V, a *J*_{sc} of 9.0 mA cm^{−2} and a FF of 52.37% was

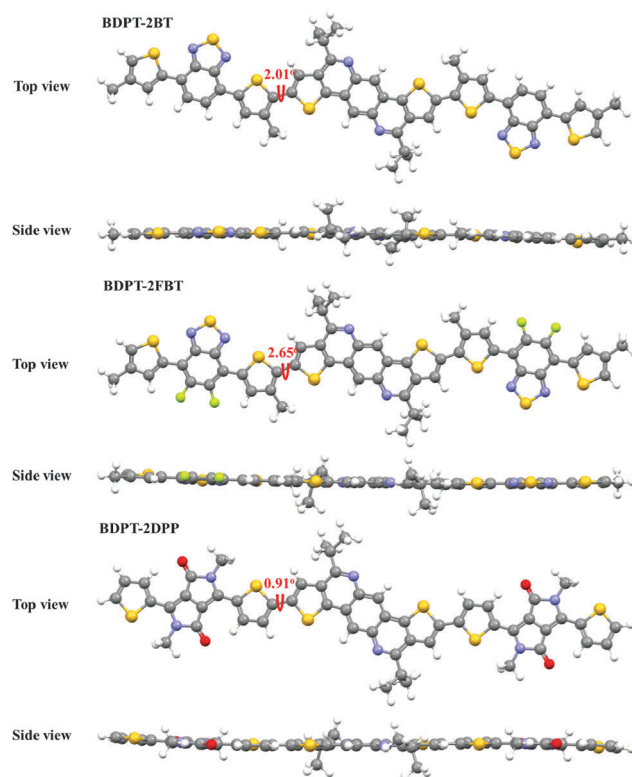


Fig. 5 Top view and side view of optimized geometries for the **BDPT**-based SMs. Color code: gray (C), white (H), red (O), blue (N), orange (S) and yellow (F).

obtained in the cell. The corresponding *J*–*V* curve is also shown in Fig. 6. The improved photovoltaic data of three SM-based devices at optimized process conditions are finally summarized in Table 2. It shows that the PCE value of the **BDPT-2DPP**-based device is 1.5 times the value of the **BDPT-2FBT**-based device.

The measurement of X-ray diffraction, photo response efficiency and hole mobility further supports why the **BDPT-2DPP**-based

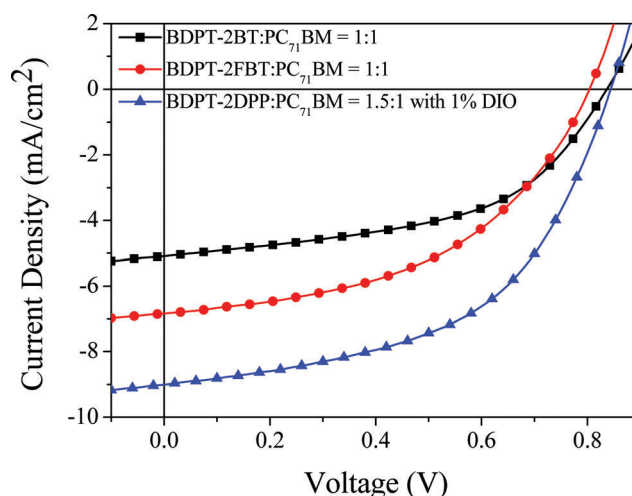
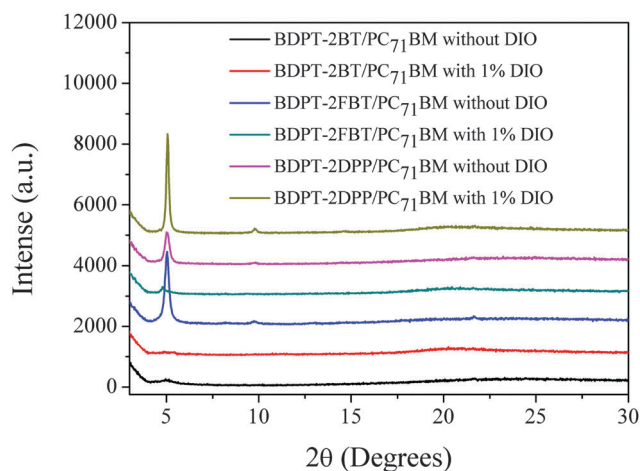


Fig. 6 *J*–*V* characteristics of the SM/PC₇₁BM-based solar cells at the blend ratio of 1 : 1.

Table 2 Photovoltaic properties of the SM/PC₇₁BM-based solar cells

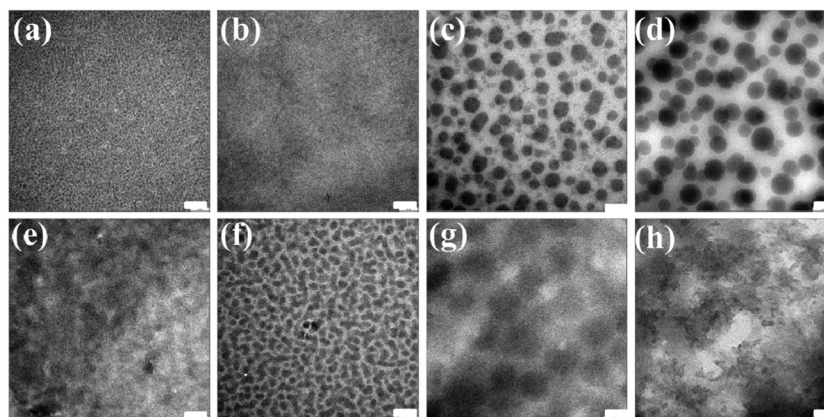
SM	D/A ratio	DIO ratio	V_{oc} (V)	J_{sc} (mA cm ⁻²)	FF (%)	PCE (%)	μ_h (cm ² V ⁻¹ s ⁻¹)
BDPT-2BT	1 : 1	No	0.84	5.08	51.25	2.18	2.94×10^{-6}
BDPT-2FBT	1 : 1	No	0.80	6.83	48.07	2.63	1.66×10^{-5}
BDPT-2DPP	1.5 : 1	1%	0.84	9.0	52.37	3.97	1.05×10^{-4}

Fig. 7 X-ray diffraction patterns of the SM/PC₇₁BM blend films with/without 1% DIO at optimized blend ratio.

device presented the best photovoltaic properties among these A₁-A-A₁ type SM-based devices. Fig. 7 shows the X-ray diffraction patterns of the SM:PC₇₁BM blend films with/without DIO additive. A clear and intense diffraction peak is observed in the **BDPT-2FBT** and **BDPT-2DPP** blend films, while the **BDPT-2BT** blend film displays a weak diffraction peak around $2\theta = 5^\circ$, which is ascribed to the diffraction between the molecular conjugated backbones separated by the branched alkyl chains. It implies that **BDPT-2FBT** and **BDPT-2DPP** have better crystallinity and self-organization than **BDPT-2BT**, which is consistent with the DSC results. When 1% DIO additive was added into the SM:PC₇₁BM blend films, the diffraction peaks disappeared for **BDPT-2BT**, weakened for **BDPT-2FBT** and were enhanced for **BDPT-2DPP** in their blend films. This indicates

that the organized nano-structure was disarranged in the **BDPT-2BT** and **BDPT-2FBT** blend films with 1% DIO additive, which resulted in the reduced PCE value. In contrast, a more ordered nano-structure was formed in the **BDPT-2DPP** blend film with 1% DIO additive. As a result, adding 1% DIO additive can significantly increase PCE and J_{sc} values of the **BDPT-2DPP**-based device.

The influence of 1% DIO additive on the film morphologies was further investigated in these blend films at the optimized ratio between the SM and PC₇₁BM by transmission electron microscopy (TEM). As shown in Fig. 8, **BDPT-2BT** and **BDPT-2FBT**-based blend films display homogeneous morphologies, but the **BDPT-2DPP**-based blend film reveals serious phase separation morphology without DIO additive. In contrast, when 1% DIO is added, an inhomogeneous morphology and a severe phase-segregation phenomenon are observed in the blend films with **BDPT-2BT** and **BDPT-2FBT**. However, homogeneous morphology with cloud-like structure appears in the **BDPT-2DPP**-based blend film under 1% DIO additive. Therefore, adding 1% DIO additive can improve the morphology of the **BDPT-2DPP**-based blend film, but destroy the homogeneousness of the **BDPT-2BT** and **BDPT-2FBT**-based blend films. In general, the inhomogeneous morphology for the photo-active layer may cause more geminate recombination and bimolecular recombination, which can decrease the J_{sc} value of the device. Proper phase separation and an interpenetrating network are beneficial for exciton separation and charge transport, which can promote the J_{sc} value of the device. This is why the **BDPT-2BT** and **BDPT-2FBT**-based devices exhibited decreased photovoltaic performances, but the **BDPT-2DPP**-based devices presented improved ones by adding the DIO additive.

Fig. 8 TEM images of the SM/PC₇₁BM blend films: (a) **BDPT-2BT**/PC₇₁BM (1 : 1), (b) **BDPT-2FBT**/PC₇₁BM (1 : 1), (c) **BDPT-2DPP**/PC₇₁BM (1 : 1), (d) **BDPT-2DPP**/PC₇₁BM (1.5 : 1) and (e) **BDPT-2BT**/PC₇₁BM (1 : 1) with 1% DIO, (f) **BDPT-2FBT**/PC₇₁BM (1 : 1) with 1% DIO, (g) **BDPT-2DPP**/PC₇₁BM (1 : 1) with 1% DIO, and (h) **BDPT-2DPP**/PC₇₁BM (1.5 : 1) with 1% DIO. The scale bars represent 200 nm.

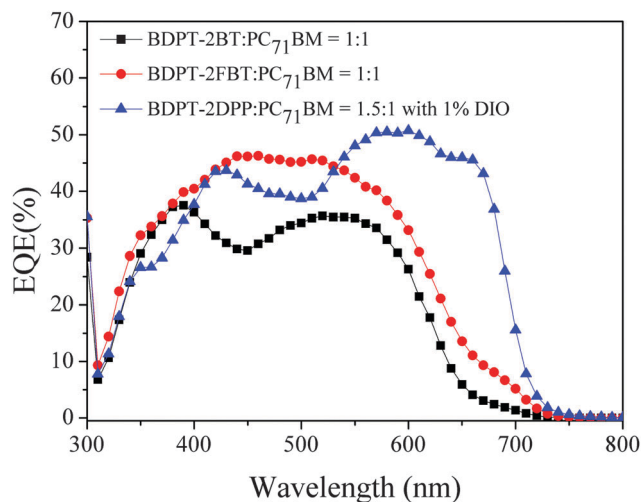


Fig. 9 EQE curves of the SM/PC₇₁BM blend films at the optimized blend ratio and DIO additive.

Fig. 9 and 10 show the EQE curves of three SM:PC₇₁BM blend films and the J - V characteristics of the hole-only devices with the SM:PC₇₁BM-based active layer, respectively. Although a similar photo response region from 300 to 650 nm is exhibited for the **BDPT-2BT** and **BDPT-2FBT** blend films, their photo response efficiencies are remarkably different. The highest EQE values of 37.5% and 45.9% are exhibited in the **BDPT-2BT** and **BDPT-2FBT** blend films, respectively. In comparison, **BDPT-2DPP** showed a broader photo response region from 300 to 710 nm with a highest EQE value of 50.6%. These calculated J_{sc} values by integration of the EQE data have only a 2–5% mismatch compared with the J_{sc} values from the J - V curve. This indicates that the photoelectron conversion process is more efficient for the **BDPT-2DPP**-based device, which is responsible for the increase in J_{sc} .

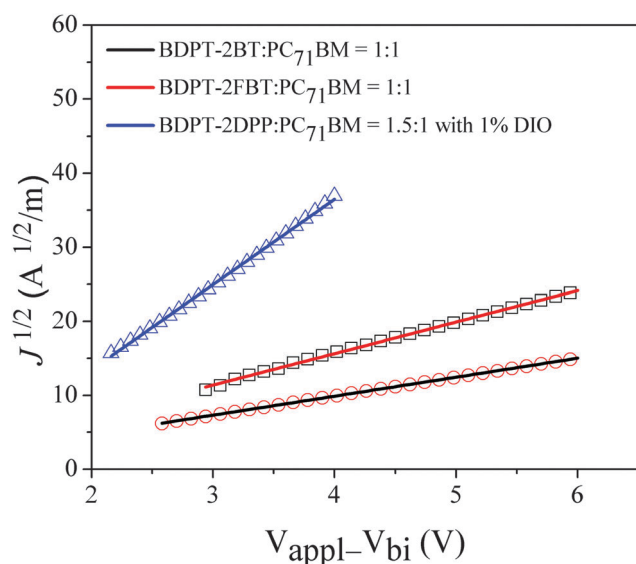


Fig. 10 J - V characteristics of the hole-only SM/PC₇₁BM-based device. The solid lines represent the best linear fit of the data points.

Fig. 10 displays J - V characteristics of the hole-only devices in the dark, in which the device structure is ITO/PEDOT/SM:PC₇₁BM/MoO₃/Al. The hole mobility was measured using a space charge limited current (SCLC) method. Hole mobilities of 2.94×10^{-6} , 1.66×10^{-5} and 1.05×10^{-4} cm² V⁻¹ s⁻¹ are presented for **BDPT-2BT**, **BDPT-2FBT** and **BDPT-2DPP**, respectively. It is obvious that the hole mobility of **BDPT-2DPP** increases by one order of magnitude compared with that of **BDPT-2FBT**, which is consistent with the improvement in J_{sc} and FF for the **BDPT-2DPP**-based device.

4. Conclusions

In conclusion, three novel A₁-A-A₁ type SMs of **BDPT-2BT**, **BDPT-2FBT** and **BDPT-2DPP** were obtained, which contain a weak and a strong electron-withdrawing acceptor unit. All of them exhibited good planarity and crystallinity, as well as low HOMO energy levels. Therein, **BDPT-2DPP** showed a broader absorption spectrum and higher photo response efficiency than **BDPT-2BT** and **BDPT-2FBT**. A maximum PCE of 3.97% with a V_{oc} of 0.84 V, a J_{sc} of 9.0 mA cm⁻² and a FF of 52.37% was obtained in the **BDPT-2DPP**/PC₇₁BM-based device. This PCE value is 1.8 and 1.5 times that of the **BDPT-2BT** and **BDPT-2FBT**-based devices, respectively. Our work demonstrates that **BDPT** is a promising weak electron-withdrawing building block for the design of photovoltaic SMs. Changing the second acceptor unit from BT to DPP can significantly improve the photovoltaic property for the A₁-A-A₁ type SMs.

Acknowledgements

Thanks to the financial support from the Major Cultivation and General Programs of the National Natural Science Foundation of China (91233112, 21172187, 51403178), the Scientific Research Fund of Hunan Provincial Education Department (10A119), the Innovation Group and Xiangtan Joint Project in Hunan Natural Science Foundation (12JJ7002 and 12JJ8001), the Natural Science Foundation of Hunan (14JJ4019), Open Project for the National Key Laboratory of Luminescent Materials and Devices (2014-skllmd-10), Research Foundation of Hunan Education Bureau (13A102, 14C1099), the Hunan Postgraduate Science Foundation for Innovation (CX2014B257, CX2013B268) and the Natural Science Foundation of Xiangtan University (13QDZ23).

References

- 1 M. Li, W. Ni, X. Wan, Q. Zhang, B. Kan and Y. Chen, *J. Mater. Chem. A*, 2015, **3**, 4765–4776.
- 2 S. Qu and H. Tian, *Chem. Commun.*, 2012, **48**, 3039–3051.
- 3 L. Ye, S. Zhang, L. Huo, M. Zhang and J. Hou, *Acc. Chem. Res.*, 2014, **47**, 1595–1603.
- 4 J. Chen and Y. Cao, *Acc. Chem. Res.*, 2009, **42**, 1709–1718.
- 5 Y. J. Cheng, S. H. Yang and C. S. Hsu, *Chem. Rev.*, 2009, **109**, 5868–5923.

- 6 R. S. Kularatne, H. D. Magurudeniya, P. Sista, M. C. Biewer and M. C. Stefan, *J. Polym. Sci., Part A: Polym. Chem.*, 2013, **51**, 743–768.
- 7 Y. Lin, H. Fan, Y. Li and X. Zhan, *Adv. Mater.*, 2012, **24**, 3087–3106, 3081.
- 8 E. Wang, W. Mammo and M. R. Andersson, *Adv. Mater.*, 2014, **26**, 1801–1826.
- 9 D. H. Wang, A. Pron, M. Leclerc and A. J. Heeger, *Adv. Funct. Mater.*, 2013, **23**, 1297–1304.
- 10 H. Choi, S. J. Ko, T. Kim, P. O. Morin, B. Walker, B. H. Lee, M. Leclerc, J. Y. Kim and A. J. Heeger, *Adv. Mater.*, 2015, **27**, 3318–3324.
- 11 Y.-J. Cheng, J.-S. Wu, P.-I. Shih, C.-Y. Chang, P.-C. Jwo, W.-S. Kao and C.-S. Hsu, *Chem. Mater.*, 2011, **23**, 2361–2369.
- 12 H. Zhou, L. Yang, A. C. Stuart, S. C. Price, S. Liu and W. You, *Angew. Chem., Int. Ed.*, 2011, **50**, 2995–2998.
- 13 T. L. Nguyen, H. Choi, S.-J. Ko, M. A. Uddin, B. Walker, S. Yum, J.-E. Jeong, M. H. Yun, T. J. Shin, S. Hwang, J. Y. Kim and H. Y. Woo, *Energy Environ. Sci.*, 2014, **7**, 3040–3051.
- 14 M. Zhang, Y. Gu, X. Guo, F. Liu, S. Zhang, L. Huo, T. P. Russell and J. Hou, *Adv. Mater.*, 2013, **25**, 4944–4949.
- 15 D. Gedefaw, M. Tessarolo, W. Zhuang, R. Kroon, E. Wang, M. Bolognesi, M. Seri, M. Muccini and M. R. Andersson, *Polym. Chem.*, 2014, **5**, 2083–2093.
- 16 L. Huo, T. Liu, X. Sun, Y. Cai, A. J. Heeger and Y. Sun, *Adv. Mater.*, 2015, **27**, 2938–2944.
- 17 J.-S. Wu, Y.-J. Cheng, T.-Y. Lin, C.-Y. Chang, P.-I. Shih and C.-S. Hsu, *Adv. Funct. Mater.*, 2012, **22**, 1711–1722.
- 18 N. Chakravarthi, K. Kranthiraja, M. Song, K. Gunasekar, P. Jeong, S.-J. Moon, W. Suk Shin, I.-N. Kang, J. W. Lee and S.-H. Jin, *Sol. Energy Mater. Sol. Cells*, 2014, **122**, 136–145.
- 19 Y. Liu, J. Zhao, Z. Li, C. Mu, W. Ma, H. Hu, K. Jiang, H. Lin, H. Ade and H. Yan, *Nat. Commun.*, 2014, **5**, 5293.
- 20 B. Kan, M. Li, Q. Zhang, F. Liu, X. Wan, Y. Wang, W. Ni, G. Long, X. Yang, H. Feng, Y. Zuo, M. Zhang, F. Huang, Y. Cao, T. P. Russell and Y. Chen, *J. Am. Chem. Soc.*, 2015, **137**, 3886–3893.
- 21 X. Guo, N. Zhou, S. J. Lou, J. W. Hennek, R. Ponce Ortiz, M. R. Butler, P. L. Boudreault, J. Strzalka, P. O. Morin, M. Leclerc, J. T. Lopez Navarrete, M. A. Ratner, L. X. Chen, R. P. Chang, A. Facchetti and T. J. Marks, *J. Am. Chem. Soc.*, 2012, **134**, 18427–18439.
- 22 M. Liu, Y. Liang, P. Chen, D. Chen, K. Liu, Y. Li, S. Liu, X. Gong, F. Huang, S.-J. Su and Y. Cao, *J. Mater. Chem. A*, 2014, **2**, 321–325.
- 23 J. Cao, Q. Liao, X. Du, J. Chen, Z. Xiao, Q. Zuo and L. Ding, *Energy Environ. Sci.*, 2013, **6**, 3224–3228.
- 24 R. Kroon, A. D. Z. Mendaza, S. Himmelberger, J. Bergqvist, O. Bäcke, G. C. Faria, F. Gao, A. Obaid, W. Zhuang, D. Gedefaw, E. Olsson, O. Inganäs, A. Salles, C. Müller and M. R. Andersson, *J. Am. Chem. Soc.*, 2014, **136**, 11578–11581.
- 25 B. He, A. B. Pun, L. M. Klivansky, A. M. McGough, Y. Ye, J. Zhu, J. Guo, S. J. Teat and Y. Liu, *Chem. Mater.*, 2014, **26**, 3920–3927.
- 26 D. Wilson, B. Djukic and M. T. Lemaire, *Transition Met. Chem.*, 2013, **39**, 17–24.
- 27 J. Chen, M. Xiao, F. Meng, L. Duan, H. Tan, Y. Wang, Y. Liu, R. Yang and W. Zhu, *Synth. Met.*, 2015, **199**, 400–407.
- 28 Y. Zhang, X. Bao, M. Xiao, H. Tan, Q. Tao, Y. Wang, Y. Liu, R. Yang and W. Zhu, *J. Mater. Chem. A*, 2015, **3**, 886–893.
- 29 P. Zhou, D. Dang, M. Xiao, Q. Wang, J. Zhong, H. Tan, Y. Pei, R. Yang and W. Zhu, *J. Mater. Chem. A*, 2015, **3**, 10883–10889.
- 30 Q. Yin, J. Miao, Z. Wu, Z. Chang, J. Wang, H. Wu and Y. Cao, *J. Mater. Chem. A*, 2015, **3**, 11575–11586.
- 31 C. Cui, W.-Y. Wong and Y. Li, *Energy Environ. Sci.*, 2014, **7**, 2276–2284.
- 32 C. L. Donley, J. Zaumseil, J. W. Andreasen, M. M. Nielsen, H. Sirringhaus, R. H. Friend and J.-S. Kim, *J. Am. Chem. Soc.*, 2005, **127**, 12890–12899.
- 33 R. S. Ashraf, A. J. Kronemeijer, D. I. James, H. Sirringhaus and I. McCulloch, *Chem. Commun.*, 2012, **48**, 3939–3941.
- 34 A. J. Kronemeijer, E. Gili, M. Shahid, J. Rivnay, A. Salles, M. Heeney and H. Sirringhaus, *Adv. Mater.*, 2012, **24**, 1558–1565.
- 35 Y. Kim, H. R. Yeom, J. Y. Kim and C. Yang, *Energy Environ. Sci.*, 2013, **6**, 1909–1916.